Available online at www.sciencedirect.com
ScienceDirect
Trans. Nonferrous Met. Soc. China 35(2025) 2521−2535
Transactions of Nonferrous Metals Society of China
www.tnmsc.cn

Solidification cracking restraining mechanism of laser-welded aluminum alloy joints using power modulation technique

Jing HAN[1], Yu SHI[1], Gang ZHANG[1], You-wei XU[1], Volodymyr KORZHYK[2], Wang-yun LE[2], Feng-xian DAI[3]

1. State Key Laboratory of Advanced Processing and Recycling of Non-ferrous Metals, Lanzhou University of Technology, Lanzhou 730050, China;
2. Zhejiang E.O. Paton Welding Technology Research Institute, Hangzhou 311200, China;
3. Zhejiang Jindan Intelligent Technology Co., Ltd., Hangzhou 311200, China

Received 29 December 2023; accepted 20 May 2024

Abstract: The 7075 aluminum alloy was subjected to power-modulated laser welding using a full-domain power modulation (FDPM) laser oscillating welding system. Three different power modes were utilized: constant power (CP), gradient power (GP), and alternating power (AP) modes. The impact of different power modes on joint crack sensitivity, microstructure, and residual stress was assessed. The results demonstrate that joint welded with the AP mode exhibits the lowest sensitivity to solidification cracking (with mean crack sensitivity of 18.3%), and the smallest average grain size in the fusion zone of the weld seam (80 μm). Additionally, it shows the highest microhardness (HV 113) and the narrowest softening region (3.5 cm). Furthermore, the joint displays the lowest residual stress and cooling rate, which is the reason for its minimal crack sensitivity.

Key words: aluminum alloy; laser welding; oscillating; crack sensitivity; power modulation

1 Introduction

The 7075 aluminum alloy is favored in aerospace, automotive, and nuclear industry applications due to its high specific strength, hardness, and excellent corrosion resistance [1,2]. Nevertheless, solidification cracking frequently occurs during the welding process [3]. This defect is influenced by various factors such as thermal shrinkage, solidification shrinkage, thermal stress or strain, inadequate filling [4], power distribution [5], and thermal cycle history of the joint [6]. Therefore, there are typically three measures to prevent thermal cracking. Firstly, from a metallurgical standpoint, a common measure is to alter the alloy composition of the weld joint by utilizing specific filling wire or additional filler materials such as scandium [7] or vanadium [8]. However, the efficacy of these methods is limited and could potentially result in a decrease in joint performance [9]. Alternatively, from a mechanical standpoint, applying additional transverse compressive strain to the metal in the brittle temperature range (BTR) during welding can help prevent cracking to some extent [10]. However, this method necessitates specific requirements for the experimental setup and platform. In contrast, implementing process control would be a highly effective approach as it mitigates the constraints associated with metallurgical and mechanical measures.

Laser welding offers several advantages, such as excellent flexibility, low heat input, minimal post-weld distortion, narrow heat-affected zone, high precision, and high efficiency [11−13]. Thus, laser welding is proven to be a viable technique for joining aluminum alloys [14]. Previous research

Corresponding author: Yu SHI, Tel: +86-13919809476, E-mail: shiyu@lut.edu.cn
https://doi.org/10.1016/S1003-6326(25)66830-0

demonstrated the significant impact of thermal conditions, including heat input and energy transfer method, on the solidification cracking in welding [15,16]. For example, using a flat-top fiber laser can influence factors such as heat input, stress, and strain, subsequently affecting the formation of cracks [17] due to its nearly ideal distribution of irradiance. Moreover, preheating has been demonstrated to reduce the strain rate in the mushy zone during pulsed laser welding of 2024 aluminum alloy, thereby decreasing the crack sensitivity [18]. HEKMATJOU and NAFFAKH-MOOSAVY [19] discovered that preheating before pulsed laser welding of 5456 aluminum alloys can decrease the cooling rate during welding. This reduction facilitates the transition from columnar to equiaxed crystals and prevents the formation of hot cracks. Similarly, altering the pulse waveform can markedly reduce the solidification rate of the molten pool, thus decreasing the probability of solidification cracks [20]. In recent years, studies have demonstrated that laser oscillating welding technology and power modulation exert a significant impact on the crack sensitivity of laser-welded joints. For instance, HAGENLOCHER et al [21] showed that laser beam oscillation can efficiently induce the formation of equiaxed grains in the welding of AA6016, thereby decreasing the sensitivity to thermal cracking. SCHAEFER et al [22] also proved that power modulation can prevent thermal cracking during laser welding of tempered steel. Although substantial advancements have been made in mitigating thermal cracking, further research is needed to investigate the intricate mechanisms of crack formation. Moreover, the development of more effective strategies for preventing thermal cracking in aluminum alloy joints is imperative.

In this work, a full-domain power modulation (FDPM) laser oscillating welding system, featuring a multi-point power adjustable function was developed. Experiments were carried out using the system to examine the laser welding of 7075 aluminum alloy in three different power modes: constant power (CP), gradient power (GP), and alternating power (AP). The main aim was to introduce a novel approach to suppress crack formation in aluminum alloy welds and analyze the underlying reasons. The proposed method provides an effective means to improve the quality of weld joints in 7xxx aluminum alloys.

2 Experimental

2.1 Materials

The material selected for the butt welding experiment was the 7075-T6 aluminum alloy, with single plate dimensions of 150 mm × 80 mm × 2 mm. This alloy comprised α-Al solid solution strengthened by a precipitated phase, predominantly the η phase ($MgZn_2$). The chemical composition of the base material is shown in Table 1, and it exhibits an ultimate tensile strength of (540±20) MPa and a yield strength of (462±18) MPa [23]. Argon gas with a purity level of 99.999% and a flow rate of 20 L/min was selected as the shielding gas. Prior to the welding process, the plate surface underwent thorough cleaning and removal of the surface oxide film through mechanical grinding. The welding procedure involved the use of a fiber laser (MFSC−6000, manufactured by Maxphotonics) operating at a wavelength of 1060 nm with a Gaussian beam diameter of 0.4 mm. A schematic diagram in Fig. 1 depicts the experimental setup, the scanning trajectory, and the power settings for the GP and AP modes. The x-direction is the welding direction, while the y-direction is perpendicular to the welding direction. In Fig. 1(c), the 36 points represent evenly spaced positions along the circular scanning path. In the GP mode, the power levels at these points exhibit a gradient pattern: at Points 1−10, the power decreases by 5%

Table 1 Chemical composition of 7075-T6 aluminum alloy (wt.%)

Si	Mn	Cu	Fe	Mg	Cr	Zn	Ti	Al
0.4	0.3	1.8	0.5	2.6	0.21	5.99	0.2	Bal.

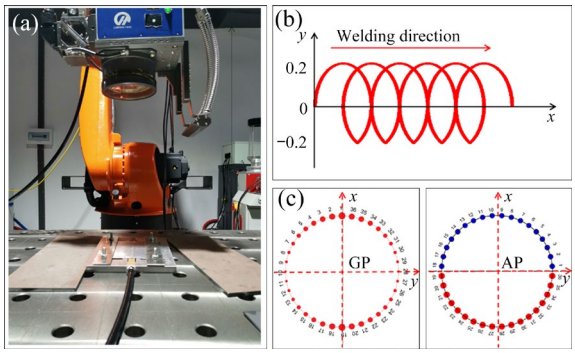

Fig. 1 Schematic diagrams of experimental device: (a) Welding equipment and fixture; (b) Scanning trajectory; (c) GP and AP mode power settings

as the beam moves away from the seam center, while at Points 10−19, the power increases by 5% as the beam approaches the center. In the AP mode, the points are segmented into two sections based on the beam position, namely the front and back ends of the weld pool. The power at the back end (Points 19−36) is 3.62 kW, while the power at the front end (Points 1−18) is 1.81 kW. To protect the laser system from potential damage due to reflection, the laser beam is angled 10° in the x−z plane towards the welding direction during the welding process. Table 2 provides detailed process parameters, where P is the laser power, P_P denotes the maximum power of the laser (P_P=6 kW), while x and y represent the coordinate positions of the beam spot along the x and y directions, respectively. A corresponds to the scanning amplitude of the beam. The average power in CP, GP, and AP modes is consistent.

2.2 Experimental conditions and settings

To assess the crack sensitivity of joints under various power modes, a Houldcroft test, also known as the "fishbone" test, was performed as it is appropriate for evaluating sensitivity to solidification cracks [24−26]. Sample specifications are illustrated in Fig. 2, showing the length of each slit in the fishbone specimen. The constraint lessens from end A to end B as the welding direction transitions from A to B. The crack sensitivity was calculated using the equation below [27]:

$$S=(L_t/L)\times 100\% \quad (1)$$

where S is the crack sensitivity (%), L_t represents the crack length (mm), and L represents the weld length (mm).

Welding experiments were conducted on the fishbone specimens using three power modes, with a minimum of three samples prepared for each group. Following welding, sampling was performed at the second location along the welding direction of the fishbone specimen. The cracked surface of the samples was then sealed and preserved for SEM photography.

The fishbone specimens and the morphology of the crack surface were examined using an optical microscope (ZEISS M2M). A detailed analysis of the microstructure of the cracked surface and the joint was conducted using the scanning electron microscopy (SEM). The elemental distribution within the joint was analyzed using the energy dispersive spectrometry (EDS) attached to the SEM. Following welding, the samples were etched in Keller reagent (2 mL HF + 3 mL HCl + 5 mL HNO_3 + 190 mL H_2O). The inductively coupled plasma spectroscopy (ICP) was employed to determine the composition of the welds. To record the thermal cycles of the weld pool, a K-type thermocouple with a probe diameter of 0.5 mm was used. Temperature data was collected using a JK808 multi-channel temperature tester, with measurement points positioned 1 mm from the weld center.

2.3 Residual stress measurement

The transverse residual stress of the joint was assessed using an X-ray residual stress tester (μ-X360n), with the (311) diffraction plane selected for the base metal. Residual stress on the plate surface was tested using the D/teX Ultra 1000 semiconductor detector employing the $\cos\alpha$ method. The collimator had a diameter of 1 mm, and the measurement step size was set at 5 mm. The final residual stress value was calculated by averaging three repeated experimental results. 21 test points were set along Line 1 in Fig. 3, including 1 point

Table 2 Detailed process parameters for welding

Welding parameter	Power mode		
	CP	GP	AP
Power/kW	2.7	$\begin{cases}P=0.58P_P(1-0.45y/A), & y\geq 0\\ P=0.58P_P(1+0.45y/A), & y<0\end{cases}$	$\begin{cases}P=0.3P_P, & x\geq 0\\ P=0.6P_P, & x<0\end{cases}$
Welding speed, v_w/(m·s^{-1})	0.02	0.02	0.02
Frequency, f/Hz	300	300	300
Amplitude, A/mm	0.2	0.2	0.2

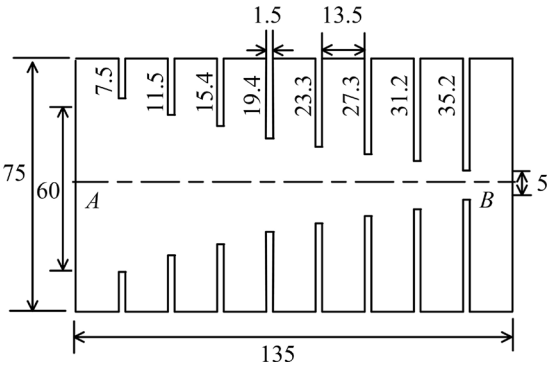

Fig. 2 Diagram of fishbone specimen (unit: mm)

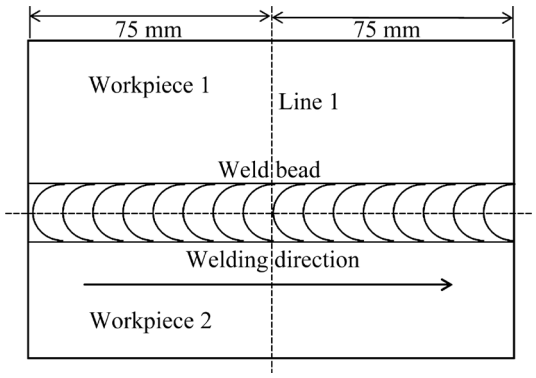

Fig. 3 Schematic diagram of residual stress measurement location

at the centerline and 10 points on each side. An oscillation unit was integrated into the testing module to optimize the measurement of residual stress.

2.4 Energy distribution calculation

During the welding process, the beam's actual trajectory follows a helical path. The equation for calculating the trajectory is as follows [28]:

$$\begin{cases} x(t)=x_0+v_{\mathrm{w}}t+A\sin(2\pi ft+\varphi_x) \\ y(t)=y_0+A\sin(2\pi ft+\varphi_y) \end{cases} \tag{2}$$

where $x(t)$ and $y(t)$ represent the horizontal and vertical coordinates of the beam spot in the coordinate system, respectively, x_0 and y_0 represent the x and y coordinates of the starting position, respectively; v_{w} is the welding speed; t is the welding time; φ_x and φ_y are the initial phases of the focal point in coordinates x and y directions, respectively; A corresponds to the scanning amplitude; f is the scanning frequency. The actual path of the scanning beam combines circular scanning and linear motion. Therefore, the scanning speed of the beam ($v(t)$) can be calculated using the following equation [29]:

$$\begin{cases} v_x=v_{\mathrm{w}}+2A\pi f\cos(2\pi ft+\varphi_x) \\ v_y=2A\pi f\cos(2\pi ft+\varphi_y) \\ v(t)=\sqrt{v_x^2+v_y^2} \end{cases} \tag{3}$$

where v_x and v_y represent the velocity components of the laser beam in the x and y directions, respectively. Based on previous research, the optimized energy distribution model of the laser beam in the oscillating welding process is represented by [30]

$$I=\frac{\eta Pv(t)}{2\pi\alpha r_0}\exp\left\{\frac{-v(t)[(x-x(t))^2+(y-y(t))^2]}{2\alpha r_0}\right\} \tag{4}$$

where I represents the energy of the laser beam, x and y are the actual positions of the beam in the x and y directions, respectively, P is the laser power, r_0 is the spot radius, η is the absorption of the laser beam by the material, and α is the thermal diffusion coefficient.

The energy of the laser irradiating on the substrate metal is given by [31]

$$E(x,y)=\int_0^T I(x,y,t)\mathrm{d}t \tag{5}$$

where $E(x, y)$ denotes the total energy of the laser beam irradiating on the metal, $I(x, y, t)$ represents the energy of the laser beam at position (x, y) and time t, and T is the scanning period. By substituting Eqs. (2) and (3) into Eq. (4), and then integrating Eq. (5), the energy distribution for different power modes can be obtained, with the values of other parameters set as follows: A=0.2 mm, r_0=0.4 mm, f=300 Hz, η=0.8, α=3.2×10^{-6} m^2/s, x_0=y_0=0, $\varphi_x-\varphi_y=\pi/2$, and v_{w}=0.02 m/s. The power values for CP/GP/AP modes are referred to Table 2.

3 Results and discussion

3.1 Energy distribution

Figure 4 illustrates the energy distribution of the three power modes over 10 cycles, with corresponding power profiles depicted. It demonstrates that in the CP mode, the energy peak is primarily situated at the edge of the melt pool (peak value: 248 J/mm^2), whereas in the GP mode, the energy peak is concentrated at the center of the melt pool (peak value: 232 J/mm^2). In the AP mode, the energy peak is focused in the region connecting

the edge and center of the melt pool (peak value: 333 J/mm^2). Interestingly, the AP mode displays a notably higher energy peak compared to the CP and GP modes, indicating superior energy concentration and heat efficiency.

3.2 Fishbone test results

During the welding process of aluminum alloys, two types of thermal cracks can occur: solidification cracks in the fusion zone and liquation cracks in the partially melted zone of the weld. Typically, solidification cracks manifest along the center of the weld, resulting in Type I cracks [32]. The morphologies of the fishbone specimens post-welding, alongside magnified images, are depicted in Fig. 5, which are identified as solidification cracks. Subsequently, the crack lengths in each specimen underwent statistical analysis, and the crack sensitivity was determined using Eq. (1). Table 3 displays notable distinctions

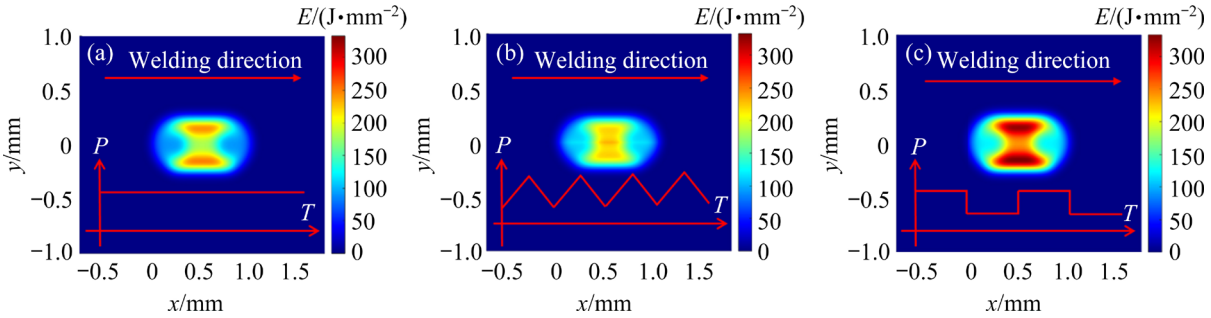

Fig. 4 Top views of energy distribution in different power modes and schematic diagrams of power profiles: (a) CP; (b) GP; (c) AP (P is the power, and T is the period)

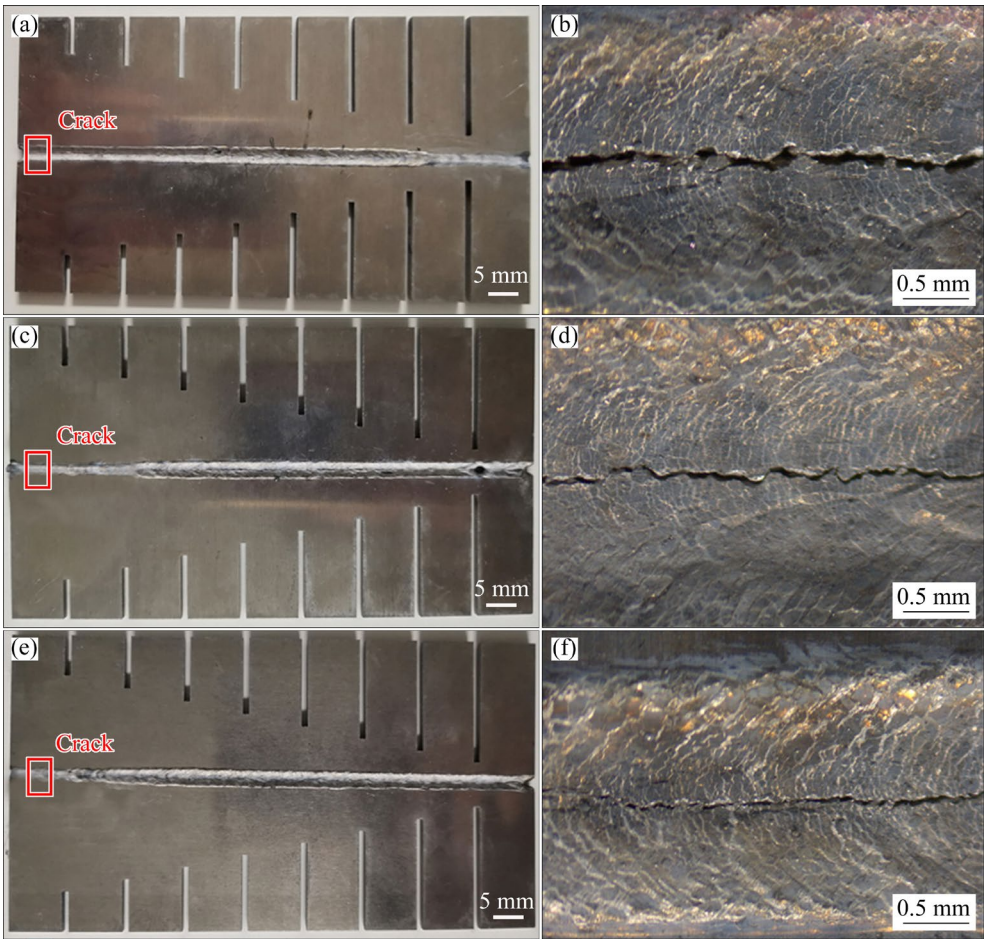

Fig. 5 Macrostructures of fishbone samples after thermal cracking sensitivity tests in different power modes: (a, b) CP; (c, d) GP; (e, f) AP

in crack sensitivity among the three modes, with the average crack sensitivities of the CP, GP, and AP mode joints being 33.1%, 27.2%, and 18.3%, respectively. The results align with the visual assessments, where the images illustrate a significant surface crack opening gap in the CP mode (Fig. 5(b)), a decreased gap in the GP mode (Fig. 5(d)), and the smallest gap in the AP mode (Fig. 5(f)).

Table 3 Results of welding thermal cracking sensitivity tests

Power mode	Crack length/mm	Crack sensitivity/%	Mean crack sensitivity/%
CP	44	32.6	33.1
	49	36.2	
	41	30.4	
GP	38	28.6	27.2
	32	25.7	
	37	27.4	
AP	24	17.8	18.3
	23	18.3	
	21	18.9	

The fracture morphologies of the cracks, as depicted in Fig. 6, show skeletal smooth dendrites without any signs of plastic deformation. The presence of such smooth dendrites is a distinctive feature of solidification cracks [33−35]. The fracture of solidification cracks typically initiates through the tearing and destruction of the intergranular liquid film. Similarly, the crack surface is seen to be coated with a layer of intergranular liquid film. Moreover, the CP mode reveals a noticeable crack in the crevice of the dendrites (Figs. 6(a, d)), while the GP mode exhibits a multitude of equiaxed dendrites (Figs. 6(b, e)). Besides the significant presence of equiaxed dendrites, the AP mode displays distinctive pulling marks on the crack surface (Figs. 6(c, f)). EDS analysis detected Al, Mg, Zn, and Cu as the primary elements present on the surface of the dendrites. This indicates the presence of eutectic phases at the grain boundaries, providing further evidence of the existence of liquid film. The observed crack morphology suggests that these cracks formed during the solid−liquid coexistence stage during the solidification process of the weld. Due to the significant amount of alloying elements present in 7075 alloy, the formation of low-melting point eutectic phases occurs more readily. As the weld seam solidifies, the primary eutectic liquid phases, including $Al_2Mg_3Zn_3$, Al_2CuMg, and $MgZn_2$, fill the spaces between grain boundaries, creating an intergranular liquid film. When the intergranular liquid film tears and breaks due to tensile stresses, solidification cracks form [36].

3.3 Microstructure

Figure 7 presents the microstructures of the fusion zone (FZ) in various power modes. It displays large-sized grains and noticeable cracks

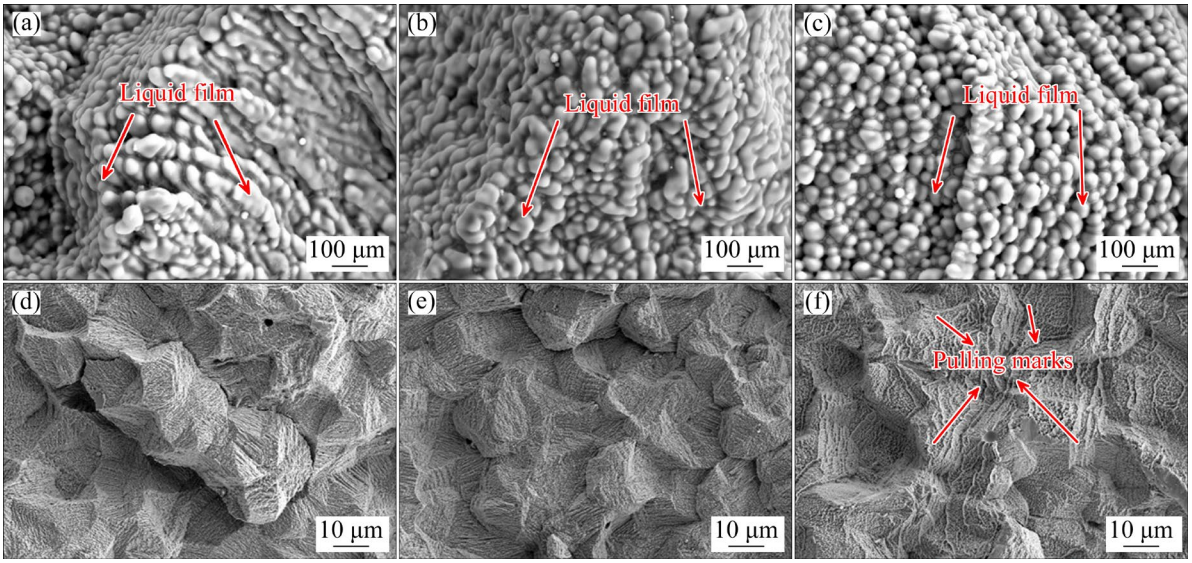

Fig. 6 Fracture morphologies of solidification cracks in different power modes: (a, d) CP; (b, e) GP; (c, f) AP

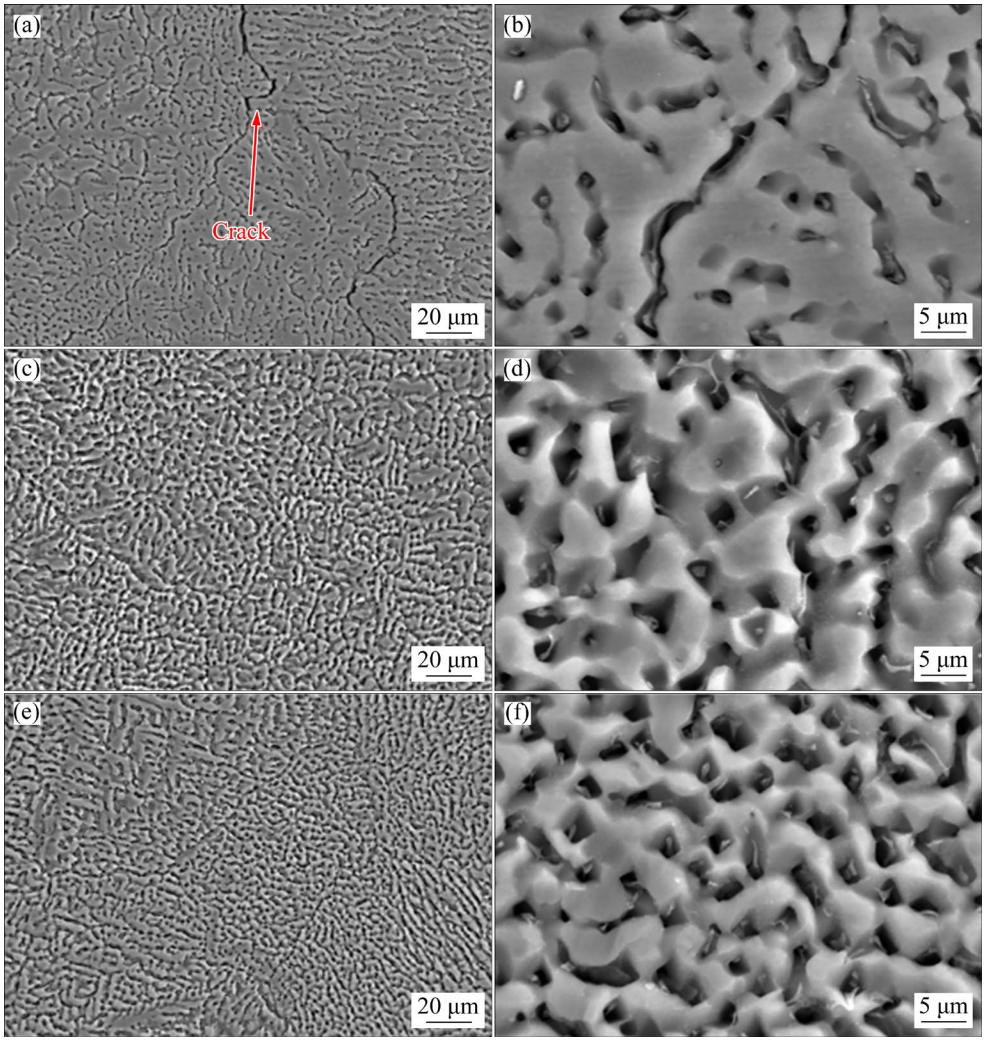

Fig. 7 Microstructures of fusion zone on cross-section of joints in different power modes: (a, b) CP; (c, d) GP; (e, f) AP

along the grain boundaries in the CP mode (Figs. 7(a, b)). The grain structure in the GP mode (Figs. 7(c, d)) closely resembles that of the CP mode. It is noteworthy that the AP mode showcases finely equiaxed grains with the highest degree of grain equiaxiality (Figs. 7(e, f)). Recent studies have explored the impact of grain size on crack sensitivity of the joints [37,38]. The results indicate that reducing grain size has the potential to decrease the coherency temperature of the material, thereby prolonging its coherency time and enhancing the coherent fraction [39]. This, in turn, reduces the accumulation of strain and decreases crack sensitivity [40]. Additionally, finer grains have been found to enhance capillary pressure [41], subsequently reducing the sensitivity of the material to solidification cracks. As a result, the AP mode joint exhibits the lowest sensitivity to cracking. MA et al [14] demonstrated that the presence of small grains decreases the local strain rate in the weld, enhances liquid permeability and backfill rate, and ultimately reduces the likelihood of cracks. The findings are consistent with the results of the current study.

Figure 8 shows the IPF maps of the joint microstructure and the grain statistics of the FZ in different power modes. The average grain size in the FZ region for joints in CP, GP, and AP modes is 92, 95, and 80 μm, respectively. Moreover, the equiaxed grains have widths of 1.6, 1.9, and 2.2 mm, respectively. These findings indicate that power modulation enhances the transition of grain morphology in the FZ from dendritic to equiaxed, with the most significant impact observed in the AP mode. Likewise, in the heat-affected zone (HAZ), the coarse columnar grains identified in the CP mode transform into fine equiaxed grains in the GP and AP modes. This transformation results in a

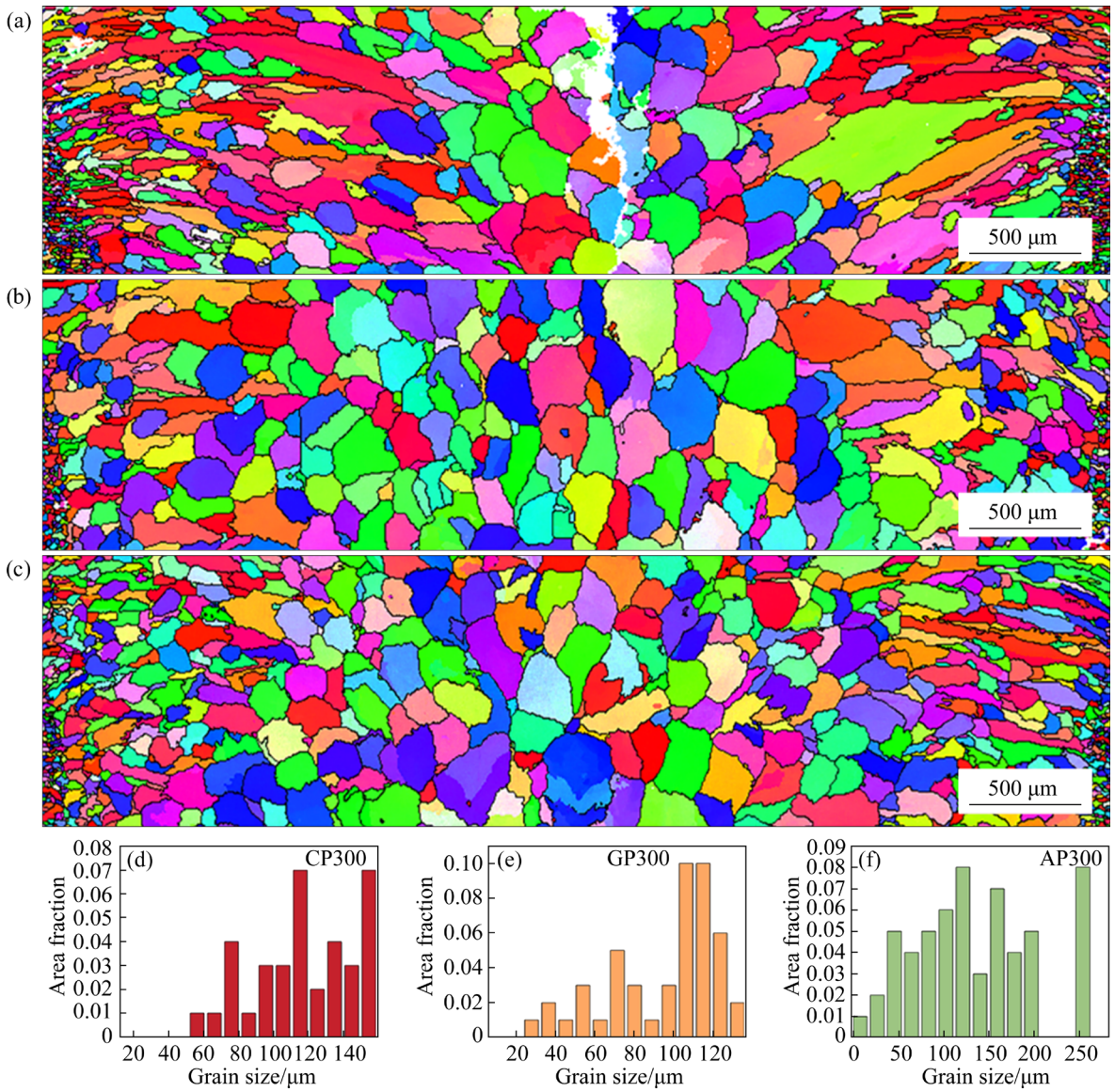

Fig. 8 IPF maps of joint microstructure and grain statistics of FZ in different power modes: (a, d) CP; (b, e) GP; (c, f) AP

notable decrease in the average grain size and a considerable enhancement in the uniformity of grain distribution. The smaller grain size observed in the FZ and HAZ of joints produced in the AP mode indicates that the AP mode is more effective than the GP mode in refining the joint microstructure.

In the overlapping section of the laser beam scanning trajectory, the preceding weld pool exerts a preheating influence on the subsequent weld pool, while the subsequent weld pool has a reheating effect on the former one. The top view of the energy distribution, as depicted in Fig. 4, reveals that the preheating and reheating impacts of the AP mode are the most pronounced. These effects diminish the cooling rate of the weld pool, augment the undercooling at the crystal growth front, and consequently elevate the heterogeneous nucleation rate, leading to a greater number of equiaxed crystals. Consequently, the AP mode displays the highest amount of equiaxed crystals in the weld seam.

The microhardness test results of welded joints in different power modes are illustrated in Fig. 9. It is evident from the figure that the microhardness of the aluminum alloy base metal is the highest at approximately HV 145.3. In the CP mode, the microhardness in the FZ of the joint is around HV 107. Comparatively, the microhardness for the joints of the GP and AP modes surpasses that of the

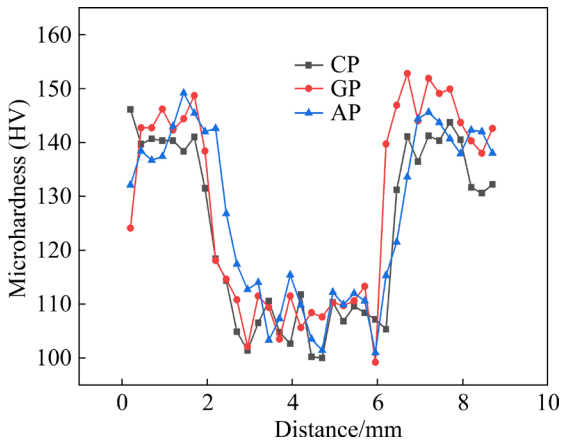

Fig. 9 Joint microhardness distribution in different power modes

CP mode. Notably, the microhardness of the AP mode joint is approximately HV 113, displaying an even distribution and marginally higher value than the GP mode (HV 109) due to the more equiaxed grains in the AP mode [42]. Besides, the width of the softened area in the FZ of the joint is measured at 4 cm in CP mode, 3.8 cm in GP mode, and 3.5 cm in AP mode. These findings indicate that power modulation reduces the softening degree of laser-welded aluminum alloy joints.

To delve deeper into the correlation between microstructure and solidification cracks, an analysis of the elemental distribution and composition of precipitated phases in the FZ of joints was conducted. As depicted in Fig. 10, the weld microstructure was found to consist of a considerable amount of gray matrix phase and dark gray spot phase. A closer analysis through elemental distribution revealed that the gray phase exhibited a high concentration of Al, whereas the dark gray spot phase showed elevated levels of Mg, Zn, and Cu. These observations indicate that the dark gray spot phase represents eutectic phases formed during the non-equilibrium solidification process [8,43,44].

In the CP mode, the levels of Al and Mg elements are relatively low. Specifically, Al element is primarily distributed within the matrix, while Mg element is uniformly distributed. Moreover, a minor amount of Zn element tends to segregate along grain boundaries, forming a low melting point eutectic phase ($MgZn_2$) with Mg element, which is a key factor in crack formation. Nevertheless, the scarce presence of the $MgZn_2$ phase in the weld hinders the development of liquid film. As a result, the intergranular liquid film fails to sufficiently resist the tensile stress engendered by weld shrinkage, thus leading to the crack formation [45]. Conversely, it has been noted that weld seams in the power modes of GP and AP show higher concentrations of Mg, Zn, and Cu elements. This indicates that the alloy elements from the base metal have diffused into the weld seam, leading to higher levels of precipitated phases and the thickening of the intergranular liquid film. A thicker liquid film requires higher stress levels to induce crack formation. Consequently, the presence of a sufficient amount of low-melting point eutectic phase has a “healing effect” on cracks. This enables the liquid to quickly fill the gaps in the dendrites,

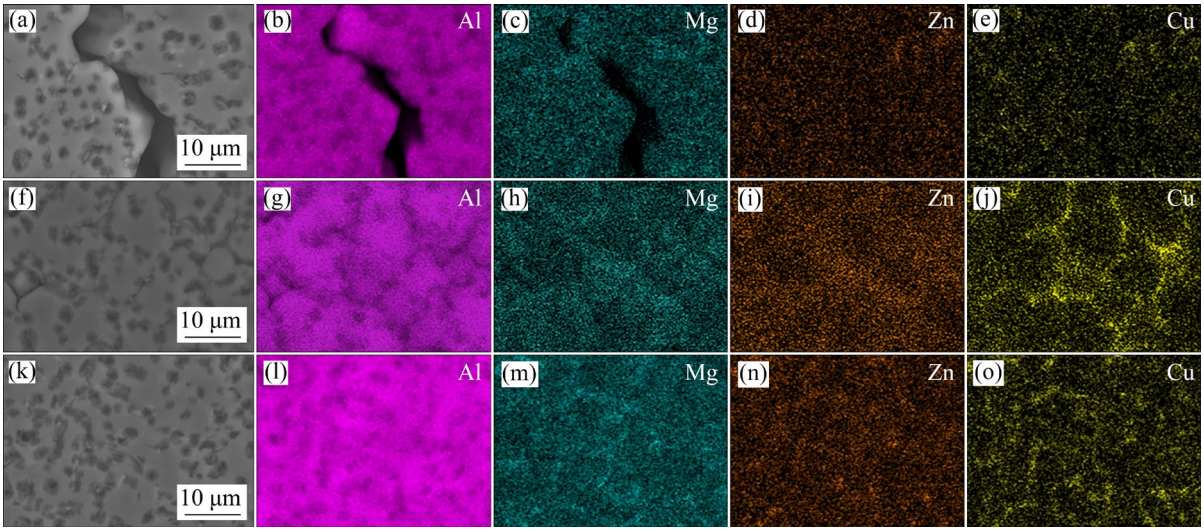

Fig. 10 Element distribution of joints in different power modes: (a−e) CP; (f−j) GP; (k−o) AP

thereby preventing thermal cracking more effectively [46,47]. In comparison to the GP mode, the grain boundary strips are dispersed in the form of short rods in the AP mode (Fig. 10(k)). It has been noted that such discontinuous and dispersed grain boundaries can withstand higher stresses, consequently mitigating cracking [25]. This phenomenon could explain the decreased sensitivity to cracking noted in the AP mode joints. The compositions of the welds, analyzed using ICP, are outlined in Table 4. The variations in elemental content among different welds demonstrate the fluctuations in the distribution of eutectic phases.

Table 4 Compositions of welds in different power modes (wt.%)

Power mode	Mg	Zn	Cu	Si	Mn	Cr	Ti	Al
CP	2.11	4.24	1.22	<0.1	<0.1	0.26	0.1	Bal.
GP	2.3	4.42	1.46	<0.1	<0.1	0.25	0.05	Bal.
AP	2.55	4.62	1.58	<0.1	<0.1	0.25	<0.05	Bal.

3.4 Residual stress distribution

Residual stress is considered as the primary factor that contributes to joint cracking, particularly in high-strength aluminum alloys. Therefore, investigating the distribution of residual stress in joints of different power modes is essential. Figure 11 illustrates the transverse residual stress distribution in the joints. The value for each point is derived from the average of three tests, with the error bar indicating the standard deviation of the repeated experiments. The distribution trend of residual stress is as follows: the weld center exhibits peak compressive stress, the HAZ experiences peak tensile stress, and there is a gradual transition from tensile stress to compressive stress from the HAZ towards both sides of the base metal. In comparison to the CP mode, both the AP and GP modes show slightly lower stress values. Particularly, the AP mode demonstrates a more significant reduction of the residual stress, facilitating a more uniform stress distribution, thus highlighting its advantages. Research suggests a correlation between the residual stress and the crack sensitivity of the joints [25]. Consequently, the residual stress variation signifies differences in crack sensitivity in different welding modes.

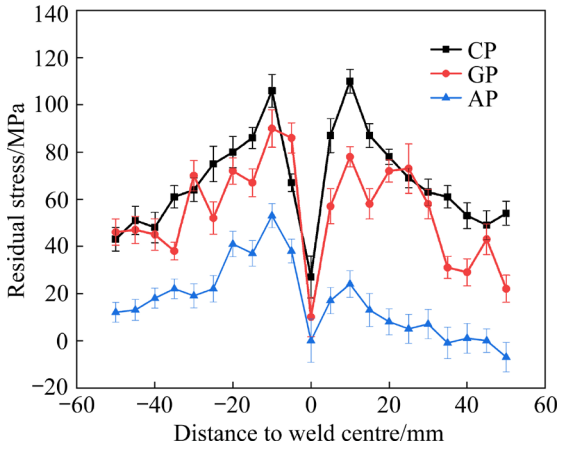

Fig. 11 Transverse residual stress distribution in joints in different power modes

3.5 Thermal cycle test results

Figure 12 displays the results of the thermal cycling of the melt pool in different power modes. The decreasing cooling rate trend during the solidification is observed as follows: AP mode < GP mode < CP mode. A lower cooling rate has been demonstrated to have three effects on the melt pool. It improves the anti-diffusion effect in the mushy zone, decreasing the level of microscopic segregation in the weld and enhancing the bridging between the α-Al dendrites. Consequently, the sensitivity to solidification cracking is reduced [48,49]. Moreover, it notably decreases the local strain rate. When the liquid backfill rate exceeds the local strain rate, the liquid backfill can compensate for the volume loss caused by the local strain, thereby preventing cracking [14]. Furthermore, a lower cooling rate leads to a reduction in grain size,

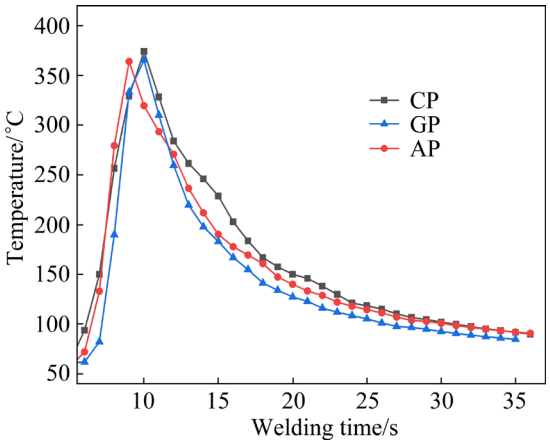

Fig. 12 Thermal cycling results of melt pool in different power modes

thereby shortening the distance for liquid backfilling and improving the efficiency of the filling process [50]. The preceding analysis illustrates that the AP mode joints exhibit the lowest sensitivity to cracking.

4 Crack sensitivity analysis results

According to KOU's model [51], the maximum value of $\mathrm{d}T/\mathrm{d}f_s^{1/2}$ serves as an indicator of cracking sensitivity for an alloy, where T is the temperature, and f_s is the solid fraction. This innovative criterion takes into account phase diagrams, solidification shrinkage, strain rate, cooling rate, and liquid filling rate. Figure 13(a) displays a longitudinal section and cross-section of two columnar grains growing in parallel along the z-direction [52]. The grain spacing is represented by ϕ, and the grain radius is denoted as R, where R is a function of the axial distance (z), expressed as $R(z)$. Assume that Grain 1 (G1) remains stationary, and Grain 2 (G2) moves towards the right at a velocity of v_{local}. To analyze the sensitivity to solidification cracking, a volume element Ω with a width of w is considered at the grain boundary. Figure 13(b) presents an enlarged image of the volume element Ω. v_{local} represents the local deformation rate that induces separation between the grains and leading to cracking. The rate at which the grains grow towards each other and prevent cracking is denoted by $\mathrm{d}R/\mathrm{d}t$. v_z represents

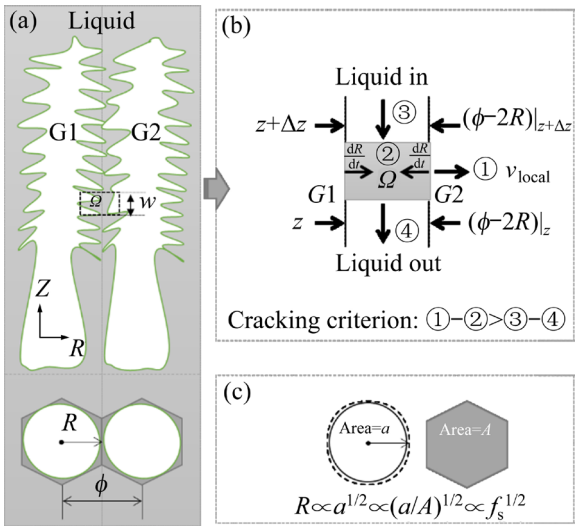

Fig. 13 Cracking criterion during weld solidification: (a) Longitudinal and cross-section of grains; (b) Enlarged image of volume element Ω; (c) Evolution of cross-sectional areas of grains during solidification

the rate at which liquid fills the grain boundary in the z-direction. The net flow rate of the liquid into the volume element Ω can be determined by subtracting the outward flow at z from the inward flow at $z+\Delta z$. In the final stages of solidification, the liquid between the grains exists as a film. If the local deformation rate v_{local} exceeds the holding capacity of the liquid film, it will lead to cracking, as indicated in Fig. 13(b). Consequently, in situations where the rate of spatial expansion exceeds the rate at which the liquid flows into the region, cracking will occur. This specifically happens if

$$w(v_{\mathrm{local}}\Delta z)-w\left[\frac{\mathrm{d}(2R)}{\mathrm{d}t}\Delta z\right]>w[((\phi-2R)v_z)_{z+\Delta z}]-w[((\phi-2R)v_z)_z] \tag{6}$$

where t signifies time. Dividing Eq. (6) by $w\Delta z$ and taking the limit as Δz approaching 0, the following expression can be obtained:

$$v_{\mathrm{local}}>\frac{\mathrm{d}(2R)}{\mathrm{d}t}+\frac{\mathrm{d}}{\mathrm{d}z}[(\phi-2R)v_z] \tag{7}$$

Figure 13(c) depicts the correlation between the growth rate of the grain ($\mathrm{d}R/\mathrm{d}t$) and the square root of the solid fraction ($f_s^{1/2}$) [52]. At the onset of solidification, the cross-sectional area of the grain is zero (marked as "a") and progresses to "A" at the end of the solidification process. Initially circular, the grain shape gradually evolves into a hexagonal structure. At the end of solidification, the liquid content within the grains becomes negligible compared to the solid phase [51]. Therefore, f_s can be accurately approximated as the ratio of a/A. Given that the grain cross-section is primarily circular, the grain radius R is directly proportional to f_s, represented as $(a/A)^{1/2}$. Hence, the relationship between the particle radius (R) and the solid fraction f_s can be elucidated as follows:

$$\frac{R}{\phi/2}=(a/A)^{1/2}=f_s^{1/2} \tag{8}$$

In order to conduct a thorough analysis of solidification processes, it is imperative to account for the solidification shrinkage factor (β). Thus, the grain radius R should be adjusted to $R(1-\beta)^{1/2}$ [51]. By substituting β, Eq. (8), and $\mathrm{d}f_s^{1/2}/\mathrm{d}t=[\mathrm{d}f_s^{1/2}/\mathrm{d}T]\cdot(\mathrm{d}T/\mathrm{d}t)$ into Eq. (7), the following equations can be derived:

$$\left\{v_{\text{local}} > \phi(1-\beta)^{1/2}\frac{\mathrm{d}f_{\text{s}}^{1/2}}{\mathrm{d}T}\frac{\mathrm{d}T}{\mathrm{d}t} + \phi\frac{\mathrm{d}}{\mathrm{d}z}[(1-(1-\beta)^{1/2}f_{\text{s}}^{1/2})v_z]\right\}_{f_{\text{s}}^{1/2}\to 1} \quad (9)$$

where $\varepsilon_{\text{local}}$ is the local strain, which is defined by the equation: $\varepsilon_{\text{local}}=D_{\text{local}}/\phi$ (D_{local} denotes the local deformation).

Dividing Eq. (9) by ϕ and defining v_{local} as $\mathrm{d}D_{\text{local}}/\mathrm{d}t$, Eq. (10) is derived [51]. The three terms in Eq. (10) correspond to the strain rate, grain growth rate, and liquid filling rate, respectively. As a result, an indicated measure of crack sensitivity in alloys during solidification is the steepness of the slope of the T–$f_{\text{s}}^{1/2}$ curve at $f_{\text{s}}^{1/2}$=0.99.

$$\left\{\frac{\mathrm{d}\varepsilon_{\text{local}}}{\mathrm{d}t} > (1-\beta)^{1/2}\frac{\mathrm{d}f_{\text{s}}^{1/2}}{\mathrm{d}T}\frac{\mathrm{d}T}{\mathrm{d}t} + \frac{\mathrm{d}}{\mathrm{d}z}[(1-(1-\beta)^{1/2}f_{\text{s}}^{1/2})v_z]\right\}_{f_{\text{s}}^{1/2}\to 1} \quad (10)$$

The T–$f_{\text{s}}^{1/2}$ curve for the aluminum alloy was constructed using the Panaluminum database in the commercial thermodynamic software Thermal-Calc. This analysis was carried out based on the Scheil solidification model without considering solid diffusion. The objective was to determine the maximum value of $|\mathrm{d}T/\mathrm{d}f_{\text{s}}^{1/2}|$. The computational results are depicted in Fig. 14. The T–$f_{\text{s}}^{1/2}$ curves display the most pronounced slope in the CP mode, followed by GP and AP. Given that materials with steeper curves are more prone to cracking during solidification, the analysis of the crack sensitivity indicator indicates that the AP joint exhibits the lowest crack sensitivity, aligning with the results from the fishbone test.

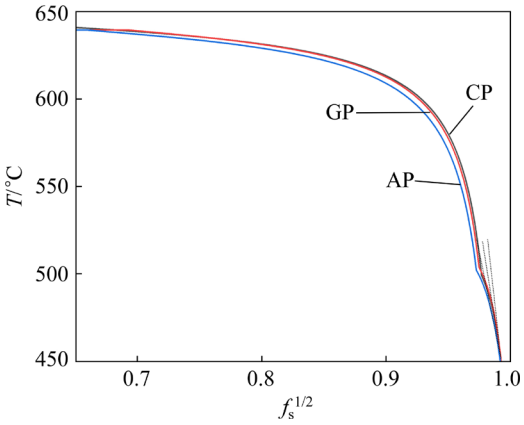

Fig. 14 T–$f_{\text{s}}^{1/2}$ curves of joints in different power modes

5 Conclusions

(1) Crack-free joints of 7075 aluminum alloy can be achieved through power modulation. The AP mode joint exhibits the lowest sensitivity to cracking, with a mean crack sensitivity of 18.3 %.

(2) The AP mode joint is characterized by the smallest average grain size of 80 μm in the FZ region. This is attributed to the preheating and reheating effects of the AP mode being the most significant in the overlapping region of the laser beam's scanning path, further leading to an increased microhardness of the joint (HV 113).

(3) The AP mode exhibits the slowest cooling rate of the weld pool, resulting in refined grain and reduced residual stress within the joint. Consequently, it displays the lowest sensitivity to cracking. These results highlight the efficacy of power modulation in mitigating thermal cracking in aluminum alloys.

CRediT authorship contribution statement

Jing HAN: Conceptualization, Methodology, Writing − Original draft preparation; **Yu SHI:** Project administration, Supervision, Resources; **Gang ZHANG:** and **You-wei XU:** Visualization; **Volodymyr KORZHYK:** Supervision; **Wang-yun LE** and **Feng-xian DAI:** Investigation.

Declaration of competing interest

The authors declare that they have no known competing financial interests or personal relationships that could have appeared to influence the work reported in this paper.

Acknowledgments

This work was supported by the National Natural Science Foundation of China (No. 52075235), the Major Science and Technology Project of Gansu Province, China (No. 22ZD6GA008), the Key Research and Development Program of Gansu Province, China (No. 20YF3WA017), the Natural Science Foundation of Gansu Province, China (No. 21JR7RA233), and the Scientific and Technological Projects of Jiayuguan, China (No. 22-16).

References

[1] CHEN Yi-wei, YANG Xu-jing, LI Mao-jun, MEI Ming. Influence of working temperatures on mechanical behavior

of hybrid joints with carbon fiber reinforced plastic/ aluminum lightweight materials for automotive structure [J]. Journal of Manufacturing Processes, 2019, 45: 392−407.

[2] RAABE D, TASAN C C, OLIVETTI E A. Strategies for improving the sustainability of structural metals [J]. Nature, 2019, 575(7781): 64−74.

[3] VICTOR CHRISTY J, ISMAIL MOURAD A, SHERIF M M, SHIVAMURTHY B. Review of recent trends in friction stir welding process of aluminum alloys and aluminum metal matrix composites [J]. Transactions of Nonferrous Metals Society of China, 2021, 31(11): 3281−3309.

[4] KOU S. Solidification and liquation cracking issues in welding [J]. JOM, 2003, 55(6): 37−42.

[5] TAN Z J, PANG B W, OLIVEIRA J P, CHEN L, BU X Z, WANG Z M, CONG B Q, ZENG Z. Effect of S-curve laser power for power distribution control on laser oscillating welding of 5A06 aluminum alloy [J]. Optics & Laser Technology, 2022, 149: 107909.

[6] LIU Yu, WANG Xin-yan, OLIVEIRA J P, HE Jing-jing, GUAN Xue-fei. Spatial and directional characterization of wire and arc additive manufactured aluminum alloy using phased array ultrasonic backscattering method [J]. Ultrasonics, 2023, 132: 107024.

[7] SOYSAL T, KOU S. Effect of filler metals on solidification cracking susceptibility of Al alloys 2024 and 6061 [J]. Journal of Materials Processing Technology, 2019, 266: 421−428.

[8] ZHANG Liang, LI Xiao-yan, NIE Zuo-ren, HUANG Hui, SUN Jian-tong. Microstructure and mechanical properties of a new Al−Zn−Mg−Cu alloy joints welded by laser beam [J]. Materials & Design, 2015, 83: 451−458.

[9] LIU Wei-ping, TIAN Xi-tang, ZHANG Xiu-zhi. A new method for prevention of weld hot cracking [J]. Transactions of the China Welding Institution, 1995, 16(2): 106−111. (in Chinese)

[10] JIANG Yu-dong. Study on controlling of welding hot cracking for aluminum alloy by welding with transverse ultrasonic [D]. Quanzhou: Huaqiao University, 2014. (in Chinese)

[11] KE Wen-chao, ZENG Zhi, OLIVEIRA J P, PENG Bei, SHEN Jia-jia, TAN Cai-wang, SONG Xiao-guo, YAN Wen-tao. Heat transfer and melt flow of keyhole, transition and conduction modes in laser beam oscillating welding [J]. International Journal of Heat and Mass Transfer, 2023, 203: 123821.

[12] ZHENG Min, YANG Jin, XU Jia-yi, JIANG Jia-wei, ZHANG Hua, OLIVEIRA J P, LV Xue-qi, XUE Jing, LI Zhu-guo. Interfacial microstructure and strengthening mechanism of dissimilar laser Al/steel joint via a porous high entropy alloy coating [J]. Journal of Materials Research and Technology, 2023, 23: 3997−4011.

[13] TESHOME F B, PENG Bei, OLIVEIRA J P, SHEN Jia-jia, AO San-san, LI Hao-yue, CHEN Long, TAN Cai-wang, SONG Xiao-guo, ZHOU Nai-xun, ZENG Zhi. Role of Pd interlayer on NiTi to Ti6Al4V laser welded joints: Microstructural evolution and strengthening mechanisms [J]. Materials & Design, 2023, 228: 111845.

[14] MA Guang-yi, YUE Kao-jie, LIU De-hua, WANG Ru-zheng, NIU Fang-yong, WU Dong-jiang. Cracking susceptibility control of 7075 aluminum alloy in pulsed laser welding with filler strip [J]. Optics and Laser Technology, 2022, 152: 108119.

[15] HOLZER M, HOFMANN K, MANN V, HUGGER F, ROTH S, SCHMIDT M. Change of hot cracking susceptibility in welding of high strength aluminum alloy AA 7075 [J]. Physics Procedia, 2016, 83: 463−471.

[16] XI Xin, LIN Dan-yang, SONG Xiao-guo, LUO Xing-shun, MA Rui, SHI Zhi-feng, BIAN Hong, FU Wei, DONG Zhi-bo, TAN Cai-wang. Strength−plasticity transition mechanism after the solution treatment of GH3230 superalloy fabricated via laser powder bed fusion [J]. Materials Science and Engineering: A, 2023, 876: 145124.

[17] ENZ J, RIEKEHR S, VENTZKE V, HUBER N, KASHAEV N. Fibre laser welding of high-alloyed Al−Zn−Mg−Cu alloys [J]. Journal of Materials Processing Technology, 2016, 237: 155−162.

[18] SHEIKHI M, MALEK GHAINI F, ASSADI H. Solidification crack initiation and propagation in pulsed laser welding of wrought heat treatable aluminium alloy [J]. Science and Technology of Welding and Joining, 2014, 19(3): 250−255.

[19] HEKMATJOU H, NAFFAKH-MOOSAVY H. Hot cracking in pulsed Nd:YAG laser welding of AA5456 [J]. Optics & Laser Technology, 2018, 103: 22−32.

[20] ZHANG Xiao-bin, CAO Zhan-yi. Effects of pulse shaping on Nd:YAG laser spot welds in an AZ31 magnesium alloy [J]. Optics and Lasers in Engineering, 2019, 119: 1−8.

[21] HAGENLOCHER C, SOMMER M, FETZER F, WEBER R, GRAF T. Optimization of the solidification conditions by means of beam oscillation during laser beam welding of aluminum [J]. Materials & Design, 2018, 160: 1178−1185.

[22] SCHAEFER M, KESSLER S, SCHEIBLE P, GRAF T. Modulation of the laser power to prevent hot cracking during laser welding of tempered steel [J]. Journal of Laser Applications, 2017, 29(4): 042008.

[23] XIAO Guan-fei, JIANG Ju-fu, WANG Ying, LIU Ying-ze, ZHANG Ying, GUO Bao-yong, HE Zhen, XIAN Xi-rui. Microstructure and mechanical properties of 7075 aluminum alloy parts formed by semi-solid thixoextrusion [J]. Transactions of Nonferrous Metals Society of China, 2023, 33(11): 3235−3249.

[24] ZHANG Yan, CHEN Gen-yu, CHEN Bing-hua, WANG Jin-hai, ZHOU Cong. Experimental study of hot cracking at circular welding joints of 42CrMo steel [J]. Optics and Laser Technology, 2017, 97: 327−334.

[25] RAMON J, BASU R, VOORT G V, BOLAR G. A comprehensive study on solidification (hot) cracking in austenitic stainless steel welds from a microstructural approach [J]. International Journal of Pressure Vessels and Piping, 2021, 194: 104560.

[26] KANNENGIESSER T, BOELLINGHAUS T. Hot cracking tests-an overview of present technologies and applications

[J]. Welding in the World, 2014, 58(3): 397−421.

[27] KOLARIK L, KOVANDA K, VALOVA M, VONDROUS P, DUNOVSKY J. Weldability test of precipitation hardenable aluminium alloy EN AW6082-T6 [J]. MM Science Journal, 2011, 2011(2): 243−247.

[28] SCHWEIER M, HEINS J F, HAUBOLD M W, ZAEH M F. Spatter formation in laser welding with beam oscillation [J]. Physics Procedia, 2013, 41: 20−30.

[29] CHEN Cong, ZHOU Hai-peng, WANG Chang-jian, LIU Li-li, ZHANG Yu-hui, ZHANG Ke. Laser welding of ultra-high strength steel with different oscillating modes [J]. Journal of Manufacturing Processes, 2021, 68: 761−769.

[30] CHEN Cong, XIANG Yun-zhong, GAO Ming. Weld formation mechanism of fiber laser oscillating welding of dissimilar aluminum alloys [J]. Journal of Manufacturing Processes, 2020, 60: 180−187.

[31] HAO Kang-da, LI Geng, GAO Ming, ZENG Xiao-yan. Weld formation mechanism of fiber laser oscillating welding of austenitic stainless steel [J]. Journal of Materials Processing Technology, 2015, 225: 77−83.

[32] GHAINI F M, SHEIKHI M, TORKAMANY M J, SABBAGHZADEH J. The relation between liquation and solidification cracks in pulsed laser welding of 2024 aluminium alloy [J]. Materials Science and Engineering: A, 2009, 519(1/2): 167−171.

[33] TIRAND G, ARVIEU C, LACOSTE E, QUENISSET J M. Control of aluminium laser welding conditions with the help of numerical modelling [J]. Journal of Materials Processing Technology, 2013, 213(3): 337−348.

[34] CHANG C C. Microstructure in hot cracking mechanism of welded aluminium alloys [J]. Materials Science and Technology, 2013, 29(4): 504−510.

[35] LIU Ren-pei, DONG Zu-jue, PAN Yong-ming. Solidification crack susceptibility of aluminum alloy weld metals [J]. Transactions of Nonferrous Metals Society of China, 2006, 16(1): 110−116.

[36] SHAO Ying-kai, WANG Yu-xi, YANG Zhi-bin, SHI Chun-yuan. Plasma-MIG hybrid welding hot cracking susceptibility of 7075 aluminum alloy based on optimum of weld penetration [J]. Acta Metallurgica Sinica, 2017, 54(4): 547−556. (in Chinese)

[37] HOSSEINI S A, ABDOLLAH-ZADEH A, NAFFAKH-MOOSAVY H, MEHRI A. Elimination of hot cracking in the electron beam welding of AA2024-T351 by controlling the welding speed and heat input [J]. Journal of Manufacturing Processes, 2019, 46: 147−158.

[38] KAH P, RAJAN R, MARTIKAINEN J, SUORANTA R. Investigation of weld defects in friction-stir welding and fusion welding of aluminium alloys [J]. International Journal of Mechanical and Materials Engineering, 2015, 10(1): 26.

[39] SPIERINGS A B, DAWSON K, KERN K, PALM F, WEGENER K. SLM-processed Sc- and Zr-modified Al−Mg alloy: mechanical properties and microstructural effects of heat treatment [J]. Materials Science and Engineering: A, 2017, 701: 264−273.

[40] RAO V R, RAMANAIAH N, SARCAR M M M. Fabrication and investigation on properties of TiC reinforced Al7075 metal matrix composites [J]. Applied Mechanics and Materials, 2014, 592: 349−353.

[41] ABDOLLAHI A, NGANBE M, KABIR A S. On the elimination of solidification cracks in fusion welding of Al7075 by TiC-nanoparticle enhanced filler metal [J]. Journal of Manufacturing Processes, 2022, 81: 828−836.

[42] YING Tao, GU Li-dong, TANG Xiao-yi, WANG Jing-ya, ZENG Xiao-qin. Effect of Sc microalloying on microstructure evolution and mechanical properties of extruded Al−Zn−Mg−Cu alloys [J]. Materials Science and Engineering: A, 2022, 831: 142197.

[43] LIU De-hua, WU Dong-jiang, WANG Ru-zheng, SHI Jing-an, NIU Fang-yong, MA Guang-yi. Formation mechanism of Al−Zn−Mg−Cu alloy fabricated by laser-arc hybrid additive manufacturing: Microstructure evaluation and mechanical properties [J]. Additive Manufacturing, 2022, 50: 102554.

[44] LIU Zhi-hao, HAN Peng, WANG Wen, GUAN Xiao-hu, WANG Zhi, FANG Yuan, QIAO Ke, YE Dong-ming, CAI Jun, XIE Ying-chun, WANG Kuai-she. Microstructure, mechanical properties, and corrosion behavior of 6061Al alloy prepared by cold spray-friction stir processing composite additive manufacturing [J]. Transactions of Nonferrous Metals Society of China, 2023, 33(11): 3250−3265.

[45] SUI Chu-fan, LIU Zheng-jun, AI Xing-yu. Effect of ultrasonic vibration on welding hot crack of 6061 aluminum alloy [J]. Transactions of the China Welding Institution, 2023, 44(1): 122−128. (in Chinese)

[46] LIU Zheng-jun, HE Si-zhuo, SU Yun-hai, ZHANG Kun. Influence of different welding materials on weldability and weld bead microstructure of 7075 aluminum alloy [J]. Journal of Shenyang University of Technology, 2018, 40(2): 139−144. (in Chinese)

[47] NONG Qi, XIE Ye-dong, JIN Chang-yi, DENG Kai-hao, SHI Qiu-hong. Research on mechanism for crystal crack forming of Al−Mg−Si alloy by Ar-arc-welding [J]. Hot Working Technology, 2013, 42(1): 205−207. (in Chinese)

[48] LIU J W, KOU S. Effect of diffusion on susceptibility to cracking during solidification [J]. Acta Materialia, 2015, 100: 359−368.

[49] Liu J W, DUARTE H P, KOU S. Evidence of back diffusion reducing cracking during solidification [J]. Acta Materialia, 2017, 122: 47−59.

[50] TANG Zhuo, VOLLERTSEN F. Influence of grain refinement on hot cracking in laser welding of aluminum [J]. Welding in the World, 2014, 58(3): 355−366.

[51] KOU S. A criterion for cracking during solidification [J]. Acta Materialia, 2015, 88: 366−374.

[52] KOU B S. A simple index for predicting the susceptibility to solidification cracking [J]. Welding Journal, 2015, 94: 374−388.

功率调制技术抑制铝合金激光焊接接头凝固裂纹的机理

韩 静[1]，石 玗[1]，张 刚[1]，许有伟[1]，Volodymyr KORZHYK[2]，乐望赟[2]，代锋先[3]

1. 兰州理工大学 省部共建有色金属先进加工与再利用国家重点实验室，兰州 730050；
2. 浙江巴顿焊接技术研究院，杭州 311200；
3. 浙江金旦智能科技有限公司，杭州 311200

摘 要：采用全域功率调制(FDPM)激光振镜焊接系统对 7075 铝合金进行功率调制激光焊接。采用 3 种不同的功率模式：恒功率(CP)、梯度功率(GP)和交替功率(AP)模式，评估了不同功率模式对接头裂纹敏感性、显微组织和残余应力的影响。结果表明，采用 AP 模式焊接的接头凝固裂纹敏感性最低(平均裂纹敏感性为 18.3%)，焊缝熔合区的平均晶粒尺寸最小(80 μm)，且接头的显微硬度最高(HV 113)，软化区域最窄(3.5 cm)。此外，AP 模式接头的残余应力和冷却速率最低，这是其裂纹敏感性最低的原因。

关键词：铝合金；激光焊接；振荡；裂纹敏感性；功率调制

(Edited by Wei-ping CHEN)